



AFRL-RX-WP-JA-2015-0125

OXIDATION BEHAVIOR OF A REFRACTORY NbCrMo_{0.5}Ta_{0.5}TiZr ALLOY (POSTPRINT)

**D.M. Dimiduk, C. Woodward, and D.B. Miracle
AFRL/RXCM**

**O.N. Senkov and S.V. Senkova
UES, Inc.**

**APRIL 2014
Interim Report**

Distribution Statement A. Approved for public release; distribution unlimited.

See additional restrictions described on inside pages

STINFO COPY

© Springer Science+Business Media, LLC 2012

**AIR FORCE RESEARCH LABORATORY
MATERIALS AND MANUFACTURING DIRECTORATE
WRIGHT-PATTERSON AIR FORCE BASE OH 45433-7750
AIR FORCE MATERIEL COMMAND
UNITED STATES AIR FORCE**

NOTICE AND SIGNATURE PAGE

Using Government drawings, specifications, or other data included in this document for any purpose other than Government procurement does not in any way obligate the U.S. Government. The fact that the Government formulated or supplied the drawings, specifications, or other data does not license the holder or any other person or corporation; or convey any rights or permission to manufacture, use, or sell any patented invention that may relate to them.

Qualified requestors may obtain copies of this report from the Defense Technical Information Center (DTIC) (<http://www.dtic.mil>).

AFRL-RX-WP-JA-2015-0125 HAS BEEN REVIEWED AND IS APPROVED FOR PUBLICATION IN ACCORDANCE WITH ASSIGNED DISTRIBUTION STATEMENT.

//Signature//

MICHEAL E. BURBA, Project Engineer
Metals Branch
Structural Materials Division

//Signature//

DANIEL J. EVANS, Chief
Metals Branch
Structural Materials Division

//Signature//

ROBERT T. MARSHALL, Deputy Chief
Structural Materials Division
Materials And Manufacturing Directorate

This report is published in the interest of scientific and technical information exchange and its publication does not constitute the Government's approval or disapproval of its ideas or findings.

Oxidation behavior of a refractory NbCrMo_{0.5}Ta_{0.5}TiZr alloy

O. N. Senkov · S. V. Senkova · D. M. Dimiduk ·
C. Woodward · D. B. Miracle

Received: 16 February 2012 / Accepted: 14 May 2012 / Published online: 6 June 2012
© Springer Science+Business Media, LLC 2012

Abstract Isothermal oxidation behavior of a refractory high-entropy NbCrMo_{0.5}Ta_{0.5}TiZr alloy was studied during heating at 1273 K for 100 h in flowing air. Continuous weight gain occurred during oxidation, and the time dependence of the weight gain per unit surface area was described by a parabolic dependence with the time exponent $n = 0.6$. X-ray diffraction and scanning electron microscopy accompanied by energy-dispersive X-ray spectroscopy showed that the continuous oxide scale was made of complex oxides and only local (on the submicron levels) redistribution of the alloying elements occurred during oxidation. The alloy has a better combination of mechanical properties and oxidation resistance than commercial Nb alloys and earlier reported developmental Nb–Si–Al–Ti and Nb–Si–Mo alloys.

Introduction

Future requirements for high-performance turbine engines inevitably include increasing thrust-to-weight ratio and more fuel efficiency. Basic principles of jet propulsion dictate fuel consumption to be a function of the fuel energy content, engine propulsion, thermal efficiency, and engine weight. The generating power of the high-pressure turbine engine improves with an increase in the turbine inlet temperature [1]. The high-pressure turbine blades that see

the highest temperatures in the engine are made from Ni-based superalloys, as these alloys have the best combination of required properties, such as creep resistance, temperature capability, environmental resistance, and damage tolerance, among all known alloys. However, operating temperatures are reaching or exceeding the theoretical limits of these materials whose melting temperatures are in the range of 1440–1600 K. Current state-of-the-art solutions to this materials problem require active or passive cooling, which increase parasitic weight and decrease overall engine efficiency. Numerous attempts to progress beyond superalloys by considering alternatives such as ceramics and intermetallics have been largely unsuccessful, because the required balance of properties, especially toughness and resistance to foreign object damage, is difficult to achieve [2]. Thus, new metallic systems with higher melting points and a good balance of structural properties at high temperatures are in high demand.

Refractory alloys such as niobium (Nb) and molybdenum (Mo) are being examined by academic and industrial groups [3–5]. High-temperature strength and creep resistance are the key properties of refractory alloys, because considerable alloy softening generally occurs at temperatures greater than $\sim 0.5–0.6 T_m$, where T_m is the absolute melting temperature. At the same time, poor room temperature ductility, poor oxidation resistance at temperatures greater than ~ 900 K, and high density limit the range of applications of these alloys.

Recently, several new refractory alloys with promising mechanical properties in a wide temperature range have been developed [6–10]. A new, so-called high-entropy alloying (HEA) approach, invented by Yeh et al. [11–13], was used to develop these new refractory alloys, which contain several principal alloying elements at near-equiatomic concentrations. These are MoNbTaW, MoNbTaWV

O. N. Senkov · S. V. Senkova · D. M. Dimiduk ·
C. Woodward · D. B. Miracle
Air Force Research Laboratory, Materials and Manufacturing
Directorate, Wright Patterson Air Force Base, OH 45433, USA

O. N. Senkov (✉) · S. V. Senkova
UES, Inc, Dayton, OH 45432, USA
e-mail: oleg.senkov@wpafb.af.mil

[6, 7], NbTaHfTiZr [8, 9], and NbCrMo_{0.5}Ta_{0.5}TiZr [10]. The high entropy of mixing and similar atomic radii of the alloying elements result in the formation of a single-phase BCC crystal structure in the first three alloys. However, the presence of Cr, having the atomic radius that is much smaller than the atomic radii of other elements in the fourth alloy, causes additional formation of a minor FCC Laves phase [10].

Because of strongly reduced diffusivity, as well as high concentration, of elements in high-entropy alloys [7, 12, 13], improved oxidation resistance may be expected. Indeed, feeding the surface layer with a sufficient amount of the alloying elements, which would form a stable oxide scale, has been considered to be the main issue during oxidation of conventional refractory alloys [14]. Heavy alloying of refractory metals with other elements, such as Al, Cr, Ti, Hf, etc., has been shown to be quite effective in obtaining remarkably improved high-temperature oxidation resistance for at least two reasons: (i) it reduces oxygen solubility and diffusivity in the matrix material and (ii) provides sufficient amount of the elements to form a stable oxide scale [15, 16]. In this study, we report on the oxidation behavior of a high-entropy refractory alloy NbCrMo_{0.5}Ta_{0.5}TiZr. A detailed analysis of the microstructure, phases, and phase compositions in differently oxidized regions provides useful information about the nature and sequence of oxidation of this complex alloy.

Experimental procedures

The NbCrMo_{0.5}Ta_{0.5}TiZr alloy was prepared by vacuum arc melting of the pure elements, as described in [10]. The actual alloy composition determined with the use of inductively coupled plasma-optical emission spectroscopy (ICP-OES) is given in Table 1. To close porosity in the as-solidified alloy, it was hot isostatically pressed (HIPd) at 1723 K, 207 MN/m² for 3 h. The crystal structure was identified with the use of a Rigaku X-ray diffractometer, Cu K α radiation, and the 2 Θ range of 5°–140°, and using the electron back-scatter diffraction (EBSD) technique. The density of the alloy was measured with an AccuPyc 1330 V1.03 helium pycnometer. The microstructure and chemical composition of phases were analyzed with the use of a scanning electron microscope (SEM) equipped with a backscatter electron (BSE), energy-dispersive X-ray

spectroscopy (EDS), and electron backscatter diffraction (EBSD) detectors. A step size of 0.2 μ m was used for simultaneous EDS and EBSD mapping.

Oxidation behavior of the alloy was studied using a TherMax 700 TGA unit (Cahn Instruments, Madison, WI). The initial sample dimensions were 4.69 \times 4.68 \times 7.66 mm³ and the sample weight was 1.3814 g. The sample in an alumina crucible was placed in a vertical furnace, heated to the temperature of 1273 K at the rate of 15 K/min, held at 1273 K for 100 h, and furnace cooled (approximately 5 10°C/min). During the whole experiment, dry air continuously flowed through the furnace at a rate of 80 ml/min. The weight of the sample was automatically registered every 20 s.

Results

Microstructure of HIPd alloy

Figure 1 shows the X-ray diffraction pattern of the HIPd NbCrMo_{0.5}Ta_{0.5}TiZr alloy. A major BCC1 phase and two minor phases, BCC2 and FCC (Laves), were identified [10]. The lattice parameters of these phases were determined to be $a = 324.76 \pm 0.16$, 341 ± 1 , and 740.0 ± 0.5 pm, respectively.

Microstructure of the HIPd alloy is shown in Fig. 2. Three characteristic constituents are clearly recognized on the backscatter electron (BSE) images. These are (i) large branching bright particles, (ii) a dark continuous matrix between the bright particles, and (iii) smaller dark particles precipitated inside the matrix. EBSD analysis indicated that both the bright particles and the dark matrix have the BCC crystal structures, whereas the dark particles have a FCC crystal structure (Fig. 3a, b). (Note that in the secondary electron (SE) image mode, Fig. 3a, the gray color code of the FCC particles is similar to the color code of large bright particles.) Although the EBSD method cannot distinguish the BCC1 and BCC2 phases, which have different lattice parameters, these phases can be identified by knowing their volume fractions. Indeed, the volume fractions of the light particles, dark particles, and the matrix were determined to be ~ 67 , 17, and 16 %, respectively. Comparing these results with the results of X-ray diffraction, one may conclude that the light particles have the BCC1 crystal structure, whereas the matrix phase has the BCC2 crystal structure. The BCC1 particles have the same

Table 1 Chemical composition of the NbCrMo_{0.5}Ta_{0.5}TiZr alloy produced by vacuum arc melting

Composition	Zr	Nb	Mo	Ti	Cr	Ta
at. %	18.48 \pm 0.37	21.84 \pm 0.43	10.04 \pm 0.020	19.40 \pm 0.39	18.39 \pm 0.38	11.86 \pm 0.24
wt %	19.36 \pm 0.38	23.30 \pm 0.46	11.06 \pm 0.23	10.67 \pm 0.21	10.98 \pm 0.22	24.64 \pm 0.49

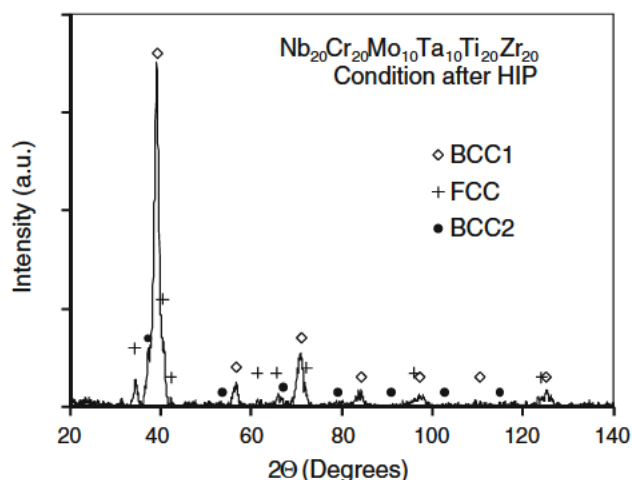


Fig. 1 X ray diffraction patterns of the NbCrMo_{0.5}Ta_{0.5}TiZr alloy after HIPing at 1723 K for 3 h

crystallographic orientation as the adjacent BCC2 matrix (Fig. 3c, e), whereas the FCC phase particles are randomly oriented and many of them are twinned (Fig. 3d, e). EDS mapping showed that these phases have different concentrations of alloying elements (Fig. 4). In particular, the concentration of Ti is much higher in the BCC2 phase than in the BCC1 phase, whereas the FCC phase has the lowest concentration of Ti (Fig. 4a). The concentration of Ta is the highest in the BCC1 phase (Fig. 4b) and Cr is mainly located in the FCC phase (Fig. 4a).

Quantitative chemical analysis of these three phases was conducted with the use of an EDS detector. The results, given in Table 2, indicate that the BCC1 phase was slightly enriched with Nb, Mo, and Ta, and depleted with Zr and Cr. The amount of Ti in the BCC1 phase is close to the average alloy composition. The BCC2 phase, on the other hand, was highly enriched with Zr and Ti and depleted with Mo, Cr, and Ta. The amount of Nb in this phase was only slightly lower of the average alloy composition. Finally, the FCC phase contained an increased amount of Cr (~41 at.%) and reduced amounts of Mo, Nb, Ta, and Ti.

Oxidation behavior at 1273 K

Continuous weight gain occurred during holding the NbCrMo_{0.5}Ta_{0.5}TiZr alloy sample at 1273 K in air (Fig. 5). The initial sample dimensions were $4.69 \times 4.68 \times 7.66$ mm³ and the sample weight was 1381.4 mg. At the time when the furnace reached 1273 K and the oxidation experiment started, the sample weight was 1397.1 mg. The weight of the sample rapidly increased during first 10 h of holding at 1273 K, but the rate of the weight increase continuously decreased with an increase in the oxidation time (Fig. 5). Such behavior can be described by a power-law dependence:

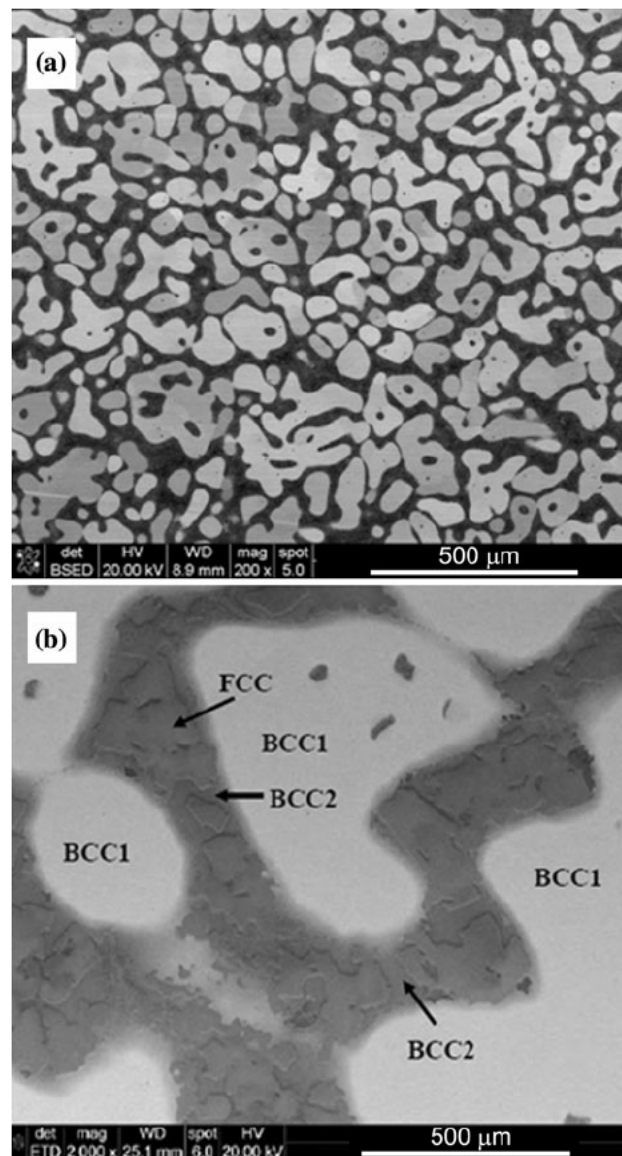


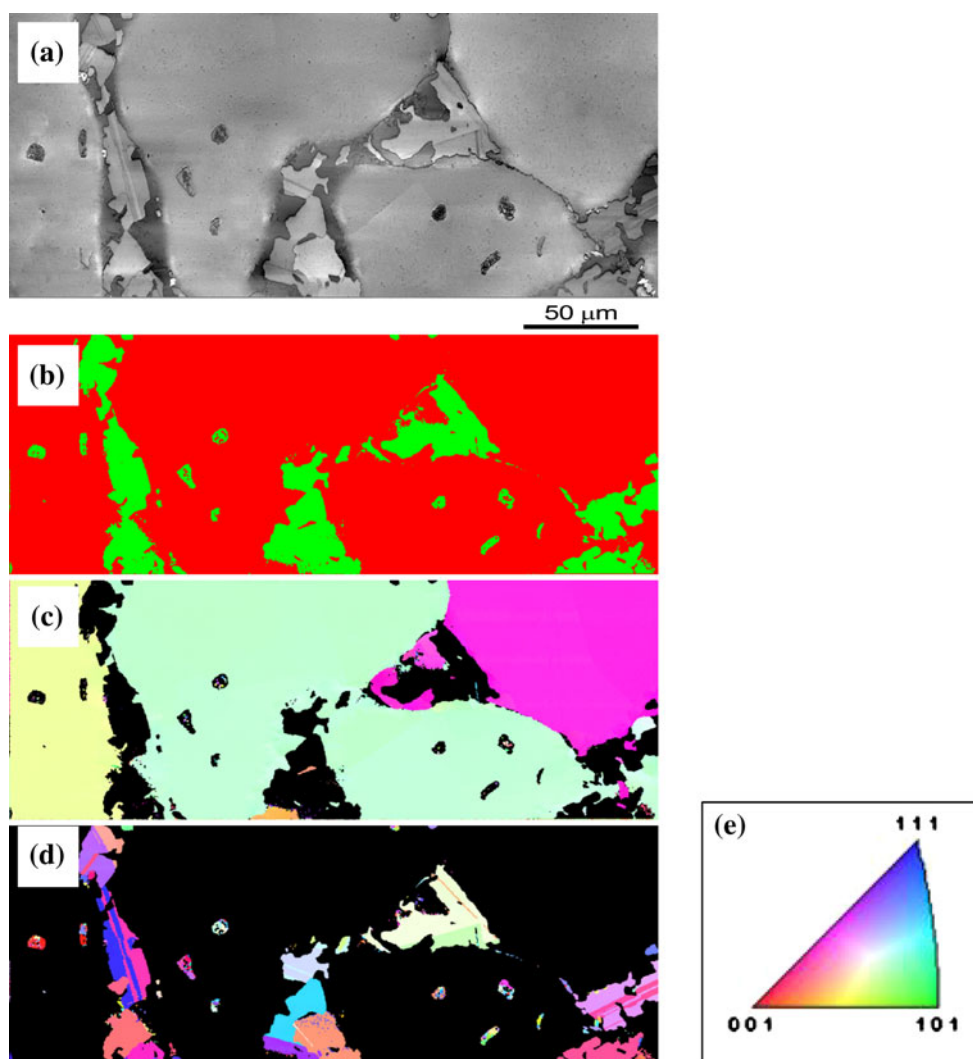
Fig. 2 SEM backscatter electron images of a polished cross section of the NbCrMo_{0.5}Ta_{0.5}TiZr alloy. **a** A low magnification image showing the duplex structure. **b** A high magnification image illustrating three phases, which have different morphologies and electron backscatter contrasts

$$\Delta m = k_1 t^n \quad (1)$$

Here, Δm is the weight gain per unit surface area, t is the holding time (in seconds) at 1273 K, n is the time exponent, and k_1 is the rate constant. The best fit to the experimental data occurs at $n = 0.6$ and $k_1 = 0.055 \text{ mg cm}^{-2} \text{ s}^{-0.6}$ (a dashed line in Fig. 5).

At the end of the experiment, after 3.6×10^5 s (100 h) holding at 1273 K, the weight of the sample was 1620.7 mg. During cooling after the high-temperature exposure, the oxide layer separated from the sample surface, likely because of different coefficients of thermal

Fig. 3 EBSD analysis of phases. **a** Secondary electron image, **b** phase map (BCC is red, FCC is green), and **c**, **d** inverse pole figure (IPF) maps of **c** the BCC phases and **d** the FCC phase. The crystallographic orientations of different grains in **c** and **d** are identified by the color scheme in the IPF triangle (**e**) (Color figure Online)



expansion of the oxide and the alloy. Six plate-like solid pieces of the oxide layer, corresponding to six rectangular surfaces of the sample, plus the remaining sample core were collected (Fig. 6). The thicknesses of these oxide pieces were approximately the same, ~ 1.75 mm, their total weight was 1016.8 mg and the volume measured by a helium pycnometer was 202.5 ± 18.2 mm³. From this data, the average oxide layer density was estimated to be $\rho_{\text{oxide}} = 5.06 \pm 0.46$ g/cm³. The remaining core dimensions were approximately $3.4 \times 3.4 \times 6.4$ mm³ at the core weight of 593.8 mg. The total weight of the recovered sample (1610.6 mg) was 10.1 mg less than the final weight of the oxidized sample measured at 1273 K. It is quite likely that few small pieces of material were left undetectable in the furnace chamber.

X-ray diffraction of the oxide layer formed on the surface of the NbCrMo_{0.5}Ta_{0.5}TiZr alloy sample during holding at 1000°C for 100 h showed that this layer consists

of many oxides (Fig. 7). Several identified oxides are Cr₂O₃, CrNbO₄, Cr₂TiO₅, Cr₂Ti₅O₁₃, CrTaO₄, MoTi-Ta₈O₂₅, Nb₂O₅, Nb₃Cr₂O₁₀, Nb₂Zr₈O₂₁, Ti₂ZrO₆, Ta₄O₅, and Ta₁₂MoO₃₃ (see Fig. 7). Other complex oxides can also be present.

Microstructure of the oxidized layer

Figure 8 shows macro-SEM/BSE images of polished cross-sections of a core (non-oxidized) part (squared shape) and a separated oxide layer of a NbCrMo_{0.5}Ta_{0.5}TiZr alloy sample after the oxidation experiment. The microstructures in the oxide layer and in the core piece look similar; however, the microstructural constituents look larger in the oxide layer, probably because of the overall expansion of the oxidized part. Higher magnification images of the oxide layer are shown in Fig. 9. The microstructure of the oxide layer repeats the microstructure of the non-oxidized alloy.

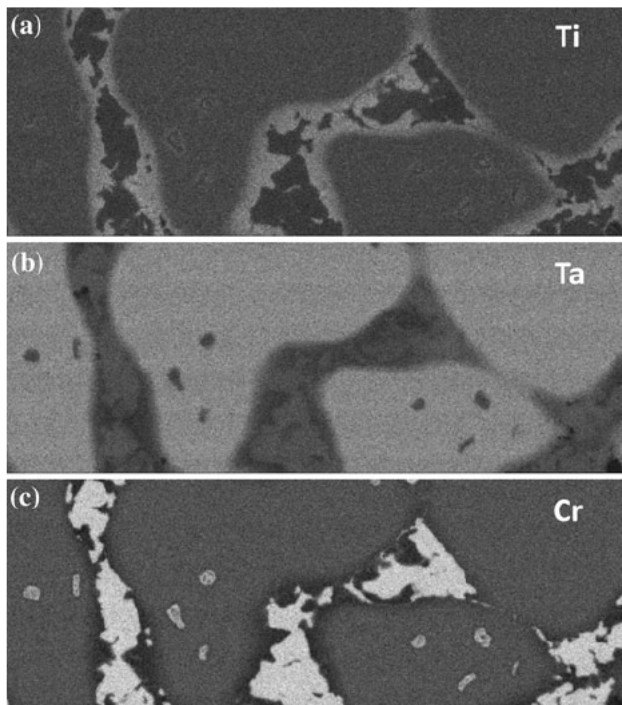


Fig. 4 EDS maps of **a** Ti, **b** Ta, and **c** Cr in different phases. The darker and lighter regions correspond to, respectively, lower and higher concentrations of the respective elements

In accord to the Z-contrast method, no noticeable redistribution of the alloying elements seems to occur. Cracks oriented almost parallel to the sample surface develop in the regions of former BCC2 and Laves phases (between former BCC1 particles). The cracks are also extended into the BCC1 particles, however in much smaller fraction, indicating that the BCC1 phase is more resistant to cracking during oxidation than the two other phases. Another plausible explanation is that the volume expansion of the BCC1 phase is larger than the expansion of other phases during oxidation. This would impose tensile strains on the remaining phases and hence their cracking. To verify this suggestion, additional in situ volume expansion experiments are required.

Figure 10 shows high-magnification BSE and SE images of a former BCC1 particle after oxidation. The images were taken at a $\times 30,000$ magnification. Different Z contrasts on the BSE image indicate that redistribution of the alloying elements occurred at a scale of less than $0.5 \mu\text{m}$

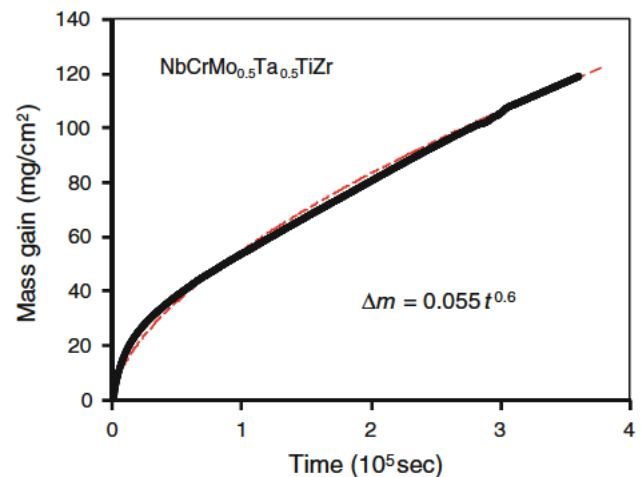


Fig. 5 The dependence of the mass gain per the initial surface area of a NbCrMo_{0.5}Ta_{0.5}TiZr alloy sample on the oxidation time during oxidation in continuously flowing dry air at 1273 K. The red dashed trendline follows the equation shown in the figure (Color figure online)

and at least three phases are present in the BCC1 particles after oxidation. These are (i) dominated gray regions, (ii) dark regions, and (iii) white elongated fine particles. The dark regions are likely to be more enriched with oxygen than the gray and light regions. Fine porosity is also present, mainly inside the dark regions. Similar phase separations are observed inside former BCC2 and FCC phases, supporting the X-ray diffraction results on the formation of many different oxides during oxidation.

The EDS analysis of the former BCC1, BCC2, and FCC phases inside the oxide layer showed about 50 at.% oxygen and noticeable variations of other elements, especially inside BCC2 and FCC phases (Table 3). To compare the compositions of oxide phases with the compositions of the respective non-oxidized phases, oxygen was excluded from counting, and the effective concentrations of the alloying elements in the oxidized phases are given in Table 4. The comparison of the phase compositions before (Table 2) and after (Table 4) oxidation gives the following information. (i) Oxidation considerably reduces the amount of Mo in all three constituents and especially in the BCC1 phase. The estimations show that the average concentration of Mo in the oxide scale is $\sim 4.4\%$ instead of 10.0% in the non-oxidized alloy. It is likely that Mo formed volatile oxides

Table 2 Chemical composition (in at.%) of the BCC1, BCC2, and FCC phases in the HIPd NbCrMo_{0.5}Ta_{0.5}TiZr alloy

Phase/element	Zr	Nb	Mo	Ti	Cr	Ta
BCC1	9.82 ± 0.29	26.80 ± 0.80	14.30 ± 0.43	19.07 ± 0.57	13.22 ± 0.42	16.80 ± 0.50
BCC2	40.60 ± 1.22	18.68 ± 0.56	0.64 ± 0.10	33.16 ± 1.10	3.09 ± 0.38	3.83 ± 0.38
FCC	23.09 ± 0.69	12.07 ± 0.36	6.35 ± 0.24	10.78 ± 0.38	40.74 ± 1.22	6.99 ± 0.21

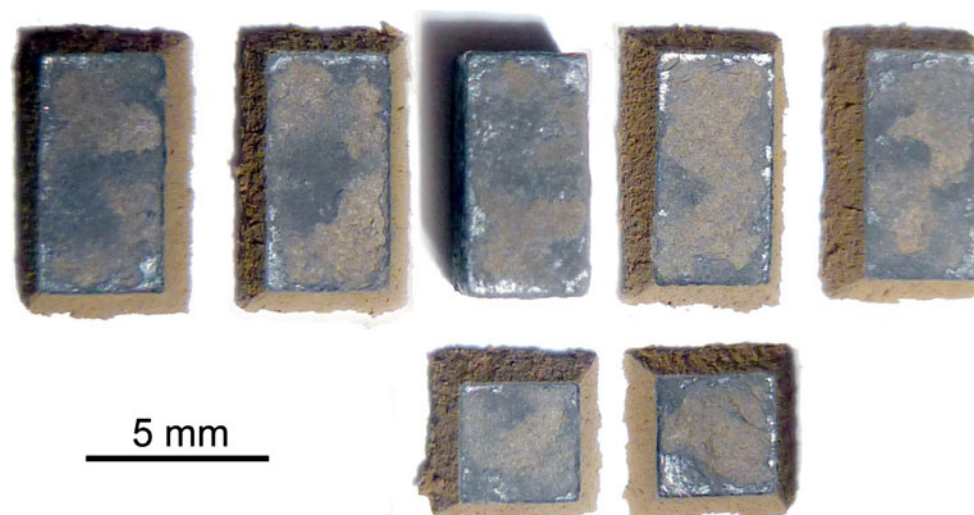


Fig. 6 A NbCrMo_{0.5}Ta_{0.5}TiZr alloy sample after oxidation in dry air at 1273 K for 100 h. During cooling from 1273 K, six pieces of the oxide layer, corresponding to six faces of the sample, separated from the remaining sample core. The *core piece* is shown in the *middle of the top row*

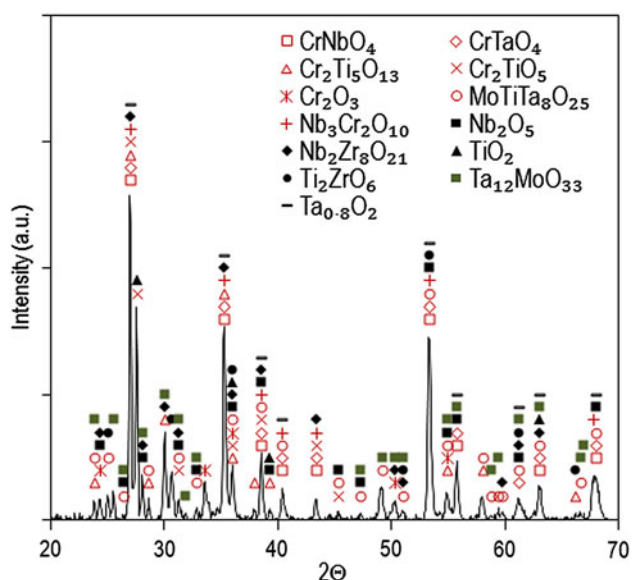


Fig. 7 X ray diffraction pattern of the oxide layer formed on the surface of the NbCrMo_{0.5}Ta_{0.5}TiZr alloy sample during holding at 1000°C for 100 h. Complex oxides are detected

which evaporated during oxidation. The presence of fine pores in the former BCC1 phase, which had high concentration (14.3 %) of Mo before oxidation, seems to support this suggestion. (ii) The concentrations of Zr, Nb, Ti, and Cr in the BCC1 phase increase proportionally to a decrease in Mo, which indicates that these four elements do not escape the BCC1 phase. (iii) A very slight (0.2 %) decrease in Ta in the former BCC1 phase is an indication that the effective concentration of Ta, relative to four other elements, is reduced in the BCC1 phase. At the same time, the concentration of Ta noticeably increases in the BCC2 phase after oxidation. It is likely that redistribution of Ta

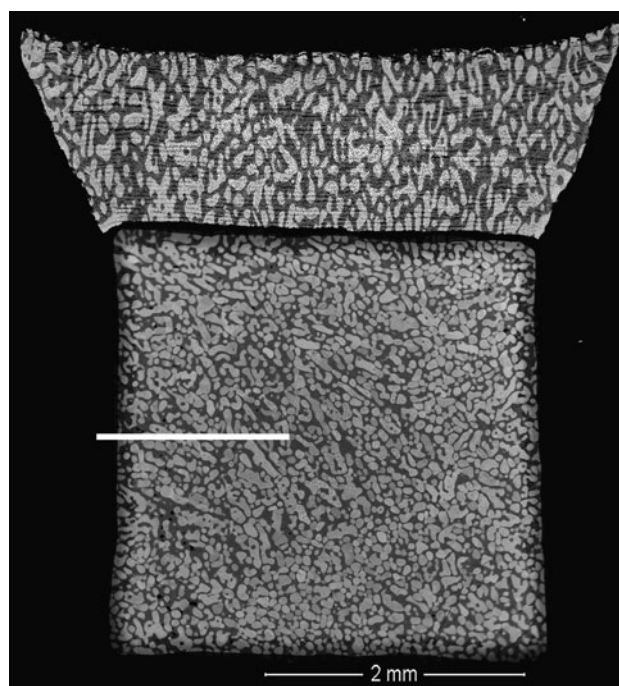


Fig. 8 Backscatter electron (BSE) image of a cross section of the core (“non oxidized”) piece (*squared shape*) and a separated oxide layer of a NbCrMo_{0.5}Ta_{0.5}TiZr alloy sample after oxidation in air for 100 h at 1273 K. The cross section of only one oxide plate (*on the top*) separated from the sample during cooling after oxidation is shown in this figure. Oxygen concentration profile was measured along the shown *white horizontal line*

between these two BCC phases occurred during oxidation. (iv) The effective concentrations of Zr and Ti decrease and Cr increase in the former BCC2 phase, but the opposite trend for these elements and almost to the same amounts is observed in the former FCC phase, after oxidation. This

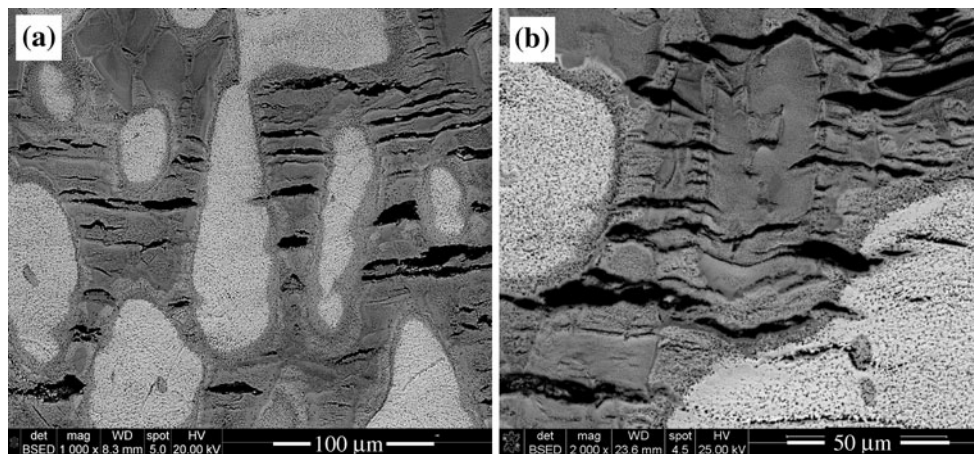


Fig. 9 Microstructure of the oxide layer. BSE images taken at different magnifications

Table 3 Chemical composition (in at.%) of the former BCC1, BCC2 and FCC phases in oxide layer

Phase\element	O	Zr	Nb	Mo	Ti	Cr	Ta
Former BCC1	51.9 ± 1.2	5.5 ± 1.0	14.1 ± 1.0	2.8 ± 0.6	10.3 ± 0.2	7.2 ± 0.5	8.2 ± 0.4
Former BCC2	50.6 ± 1.2	17.6 ± 3.0	9.7 ± 1.5	0.0	14.5 ± 2.0	4.4 ± 1.2	3.3 ± 0.5
Former FCC	48.8 ± 1.2	13.5 ± 2.7	8.1 ± 1.5	1.3 ± 1.3	7.1 ± 1.5	17.4 ± 7.0	3.9 ± 0.8

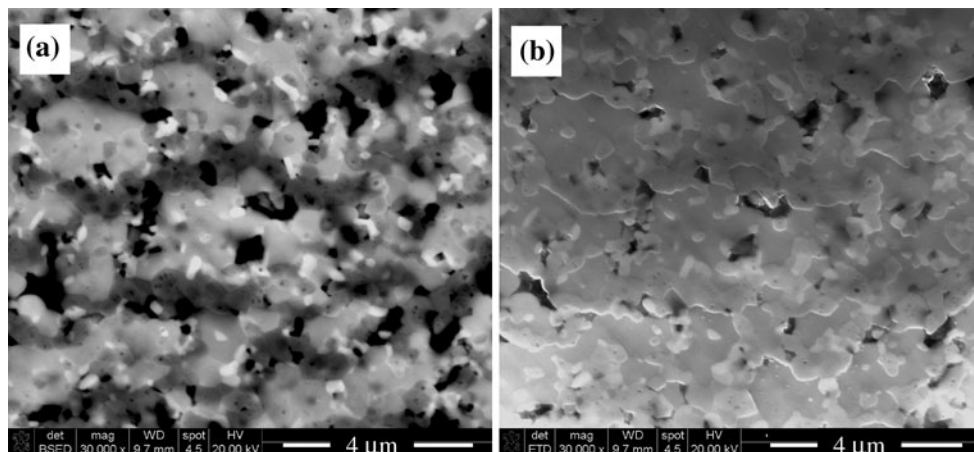


Fig. 10 **a** BSE and **b** SE images of the former BCC1 particle after oxidation

may indicate that redistribution of these elements between BCC2 and FCC phases occurred at 1273 K, which is fixed by the oxidation event.

Microstructure of the core part

The secondary and backscatter electron images of the microstructure of the under-surface region of the core part of the oxidized sample are shown in Fig. 11a, b, respectively. Two layers above the non-oxidized matrix are clearly identified. These are (i) a remaining (non-split), ~5–80-μm thick, complex oxide layer and (ii) a transition,

~120–160-μm thick, partially oxidized layer. The microstructure and chemistry of the complex oxide layer are similar to those described in Sect. 3.3. The microstructure and chemistry of the transition layer are different and thus can provide additional information on kinetics of oxidation.

A representative microstructure of the transition layer under the oxide scale is shown in Fig. 12 and chemical compositions of different regions, identified in Fig. 12, are given in Table 5. Locations of former BCC1 (regions 1 and 2 in Fig. 12), BCC2 (regions 3 and 4), and Laves phases (region 5) are clearly distinguished. During oxidation, the BCC2 phase transforms into a lamellar structure consisting

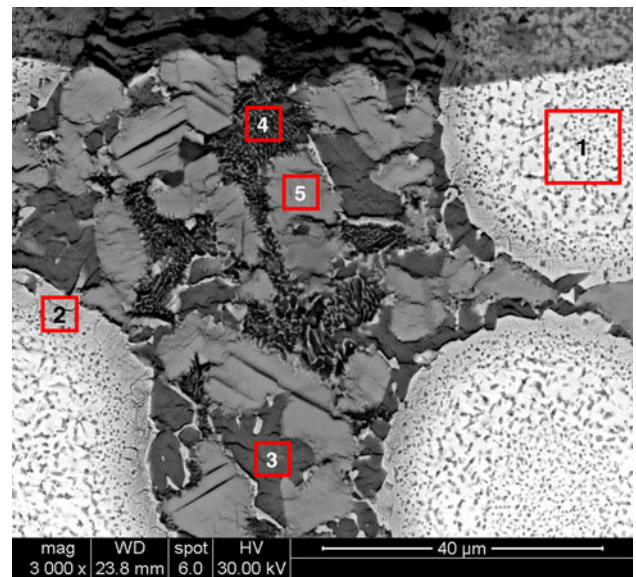
Table 4 Effective concentrations of the alloying elements (in at.%) in the former BCC1, BCC2 and FCC phases in the oxide layer, without counting oxygen

Phase\element	O	Zr	Nb	Mo	Ti	Cr	Ta
Former BCC1		11.4 ± 2.0	29.3 ± 2.0	5.9 ± 1.2	21.5 ± 0.4	14.9 ± 1.0	17.0 ± 0.8
Former BCC2		35.6 ± 6.0	19.6 ± 3.0	0.0	29.3 ± 4.0	8.8 ± 2.4	6.6 ± 1.0
Former FCC		26.3 ± 5.4	15.8 ± 3.0	2.6 ± 2.6	13.8 ± 2.9	33.9 ± 13.6	7.6 ± 1.6

of at least two components: dark oxide phase with an increased Zr content and a bright, less oxidized phase, which has the chemistry of the BCC1 phase. Oxidation of the Laves phase (gray particles, similar to region 5 in Fig. 12) leads to formation of sharp, almost linear cracks, some of which are parallel to each other or meet at $\sim 120^\circ$ angle within one particle. These morphological features may indicate that the cracks cut the particles along specific crystallographic directions, though no special crystallographic analysis was conducted. Oxidation of the Laves phase particles occur evenly and no visible phase separation is seen inside these particles. The surface layer of former BCC1 particles (region 2) becomes darker, and small radial cracks form at this layer due to enrichment with oxygen. This analysis indicates that, among three phases presented in the alloy, the BCC1 phase is the most resistant and the BCC2 phase is the least resistant to oxidation. Oxidation of the Laves phase leads to cracking, whereas oxidation of the BCC2 phase initiates eutectic reaction with the formation of at least two oxide phases.

The microstructure of the central region of the core part is given in Fig. 13. No oxygen is present in this region and the chemical compositions of the BCC2 and FCC phases are similar to the non-oxidized alloy. Fine precipitates are formed inside the primary BCC1 particles. The EBSD analysis indicates that these precipitates have the FCC structure and are likely the Laves phase [10].

Oxygen distribution inside the core part along the horizontal line shown in Fig. 8 is given in Fig. 14 (*solid white line*). The negative distance values at the horizontal axis correspond to mount material (plastic) and the positive values correspond to the distance from the sample surface.

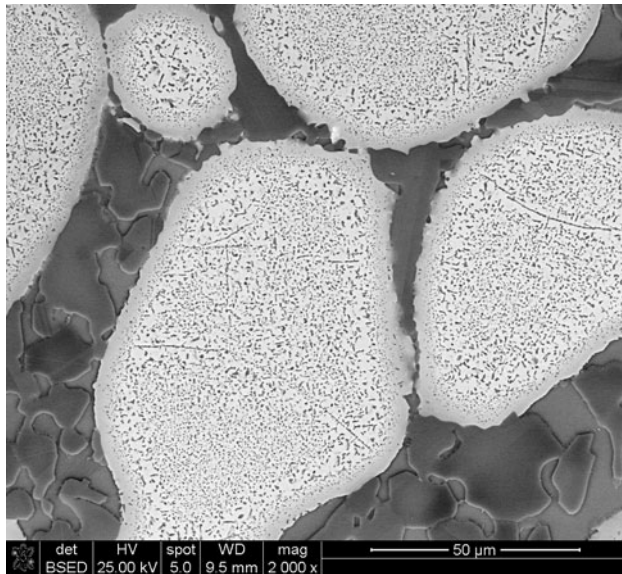
Fig. 11 a SE and b BSE images of the under surface transition region of the core part of the oxidized sample**Fig. 12** A BSE image of the transition (partially oxidized) region of the core part. Areas are shown, from which chemical compositions were determined

The oxygen concentration is maximum at the sample surface, it exponentially decreases with an increase in the distance from the surface inside the sample, and is zero at the distances of $\sim 150 \mu\text{m}$ and above. This concentration profile can be described as a sum of two Gaussian distributions, $C_O = A \exp[-(x/\sigma)^2/2]$, where x is the distance from the sample surface and σ is the standard deviation. For the first Gaussian (Gauss1 in Fig. 14), $\sigma_1 = 10 \mu\text{m}$, and for the second Gaussian (Gauss2), $\sigma_2 = 50 \mu\text{m}$. Two Gaussian distributions can be because of different

Table 5 Chemical composition (in at.%) of different regions (shown in Fig. 12) in the transition (partially oxidized) layer

Phase/element	O	Zr	Nb	Mo	Ti	Cr	Ta
1. Former BCC1, center	8.84 (0.00)	15.0 (16.5)	17.5 (19.2)	7.75 (8.50)	20.0 (21.9)	18.2 (20.0)	12.7 (13.9)
2. Former BCC1, surface layer	18.5 (0.00)	9.77 (12.0)	20.7 (25.4)	12.0 (14.7)	15.5 (19.0)	10.6 (13.1)	13.0 (15.9)
3. Former BCC2 (dark)	38.6 (0.00)	36.7 (59.8)	7.37 (12.0)	0.56 (0.91)	7.71 (12.6)	7.26 (11.8)	1.78 (2.90)
4. Former BCC2 (eutectic)	37.0 (0.00)	24.3 (38.6)	11.4 (18.1)	0.53 (0.84)	22.9 (36.4)	1.70 (2.70)	2.16 (3.43)
5. Former FCC	22.7 (0.00)	18.0 (23.2)	9.16 (11.9)	5.52 (7.14)	7.12 (9.21)	32.0 (41.5)	5.51 (7.13)

Effective concentrations of main alloying elements, without counting oxygen, are given in brackets. The numbers in the first column correspond to the respective outlined regions in Fig. 12. The experimental error is $\sim 7\%$

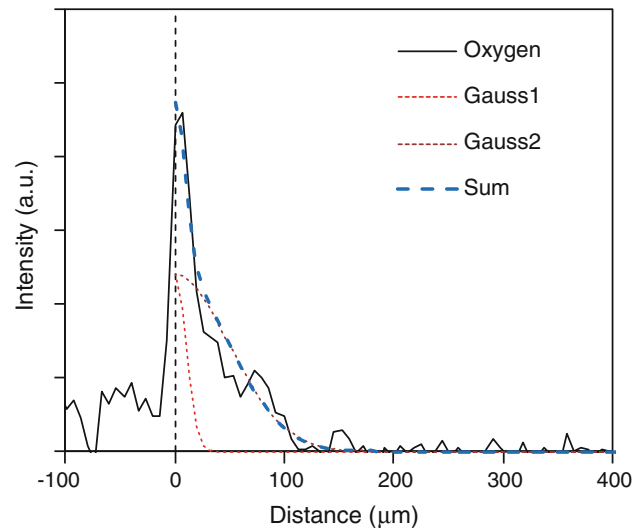
**Fig. 13** Microstructure of a non oxidized core part after holding for 100 h at 1273°K

diffusivity of oxygen inside the BCC1 particles and in the BCC2 matrix (and in the Laves phase). Taking into account that $\sigma^2 = 2Dt$, where D is the coefficient of diffusion and t is time, one can conclude that the diffusion of oxygen in the BCC1 phase is ~ 25 times slower than in the BCC2/Laves phases.

Discussion

Oxidation kinetics

There are two extreme conditions for the oxidation reaction of metallic alloys [17–19]. The first condition occurs when oxygen is in direct contact with the surface and the rate-controlling mechanism for the oxidation reaction is a gas metal interface reaction. In this case, the mass gain per unit surface area linearly increases with the oxidation time and the time exponent, n , in Eq. (1) is equal to unity ($n = 1$). Oxidation by this mechanism generally occurs when the

**Fig. 14** The oxygen concentration profile (solid dark line) inside the core part along the horizontal line shown in Fig. 8. The dashed vertical line corresponds to the oxide/core matrix interface. The profile can be described as a sum of two Gaussian distributions, $C = A \exp[-(x/\sigma)^2/2]$, where x is the distance from the interface and σ is the standard deviation. For the first Gaussian (Gauss1), $\sigma_1 = 10 \mu\text{m}$, and for the second Gaussian (Gauss2), $\sigma_2 = 50 \mu\text{m}$

surface oxide is unable to form a continuous passive layer and retard further oxidation of the substrate alloy because of different reasons, such as (a) a smaller oxide volume than the volume of the alloy from which it forms, (b) low vapor pressure and easy evaporation of oxide products, (c) instability of the oxide because of high oxygen solubility and high oxygen transport rates in the matrix, and/or (d) continuous spallation.

The second extreme condition occurs when a crack-free stable surface oxide film forms, which protects the alloy from direct contact with gaseous oxygen, and diffusion through the oxide layer becomes the rate-controlling process for the oxidation reaction. In this case, the oxidation rate (i.e., the rate of the mass gain per unit surface area) decreases with time, and $n = 0.5$. This situation takes place when the volume of the forming surface oxide is the same or larger than the volume of the alloy participating in the reaction and the oxide is well adhered to the matrix [19, 20].

During oxidation in continuously flowing air at 1273 K, the new refractory alloy NbCrMo_{0.5}Ta_{0.5}TiZr showed a near-parabolic dependence of the mass gain per unit surface area on the oxidation time, with an overall time exponent $n = 0.6$ (see Fig. 5). This value of n is close to $n = 0.5$ indicating diffusion controlling formation of a protective oxide layer. Indeed, naked eye and mass balance examination, as well as the microstructure analysis, of the oxidized sample revealed formation of a rather solid and dense oxide layer with no radially directed cracks and no oxide spallation during the oxidation process. When the dependence of the mass gain per unit surface area on the oxidation time is plotted in the logarithmic coordinates, two distinct behaviors can clearly be seen (Fig. 15). During the first 1500 s (~ 25 min), oxidation is fast and $n = 0.85$. In the time range from ~ 1500 to 3600 s (25–60 min), the oxidation rate decreases, n decreases to $n = 0.5$ and keeps this value until the end of the experiment. This analysis indicates that (a) during the first 25 min, the alloy oxidation is controlled mainly by the oxygen alloy interface reaction process, (b) within the first 60 min, the alloy surface is completely covered by a stable oxide film, and (c) further oxidation is controlled by the oxygen diffusion through this oxide film.

Fine porosity observed inside the former BCC1 particles after their oxidation may accelerate the oxygen diffusion and oxidation kinetics. Fortunately, these particles are isolated from each other by the continuous BCC2 phase, which forms continuous oxide network around the porous oxide particles. No porosity was observed in the oxidized BCC2 and Laves phases. It is also necessary to point out that, although the accelerated oxygen diffusion may occur through the porous oxidized particles, the oxidation rate of

these particles was much slower than that of the BCC2 phase and thus the average rate of the oxygen diffusion through these particles may not be very much different from the oxygen diffusion rate through other phases.

The density of the oxide, $\rho_{\text{oxide}} = 5.06 \pm 0.46$ g/cm³, is about 38.5 % smaller than the density of the alloy, $\rho_{\text{alloy}} = 8.23 \pm 0.01$ g/cm³ [10], which is associated with considerable volume expansion during oxidation. Indeed, assuming that the core (under the oxide layer) part of the sample does not change volume during oxidation, the initial volume of the surface layer, which transformed to the oxide, is estimated to be $V_{\text{SL}} \approx 94.1$ mm³. After oxidation, this layer expanded to $V_{\text{SO}} = 202.5$ mm³, i.e., more than two times.

By knowing the mass of the oxidized surface layer before ($= \rho_{\text{alloy}} \times V_{\text{SL}} \approx 773.9$ mg) and after (1016.8 mg) oxidation and the molar weights of the alloy (87.09 g/mol) and oxygen (16.0 g/mol), molar fractions of the metal atoms (i.e. alloying elements, Me) and oxygen (O) in the oxide layer can be estimated. Indeed, the amounts of metal and oxygen atoms in the oxide layer are estimated to be $N_{\text{Me}} = 0.0089$ mol and $N_{\text{O}} = 0.015$ mol, respectively, which gives the mole fractions of metals and oxygen of ~ 0.37 and 0.63 . These fractions are close to the oxide formula Me_3O_5 , which can be considered as a mixture of MeO , MeO_2 , and Me_2O_3 oxides ($2\text{Me}_3\text{O}_5 = \text{MeO} + 3\text{MeO}_2 + \text{Me}_2\text{O}_3$). These estimations of the amount of oxygen in the oxide layer are noticeably higher than ~ 50 at.% experimentally determined by EDS. This discrepancy may indicate that the weight gain was because of not only the reaction with oxygen but also because of nitrogen pickup (nitrating). Unfortunately, nitrogen was not within the list of the elements analyzed by EDS, because its $K\alpha$ line was shielded by the $L\alpha$ line from Ti.

It is necessary to point out that the above analysis did not take into account evaporation of some molybdenum oxides during the oxidation experiment. Indeed, it was found in this study that the oxide scale contains a reduced amount of Mo (about 56 % reduction relative to the amount in the non-oxidized alloy), which is likely an indication that some molybdenum escaped the oxide scale by forming volatile oxides. The evaporation of molybdenum oxides effectively reduces the weight of the oxidized sample, and this weight loss should be taken into account for the correction of the sample weight gain with time. The total weight of the Mo escaped from the oxide scale is estimated to be ~ 47.9 mg. Assuming that MoO_2 oxide forms at $T = 1273$ K, the total weight of the escaped MoO_2 is then estimated to be ~ 63.9 mg. Thus, the total weight of the oxidized sample should be increased from the measured 1620.7 mg to the oxide-loss corrected 1684.5 mg. To make corresponding corrections to the kinetics of oxidation of the studied alloy, the kinetics of

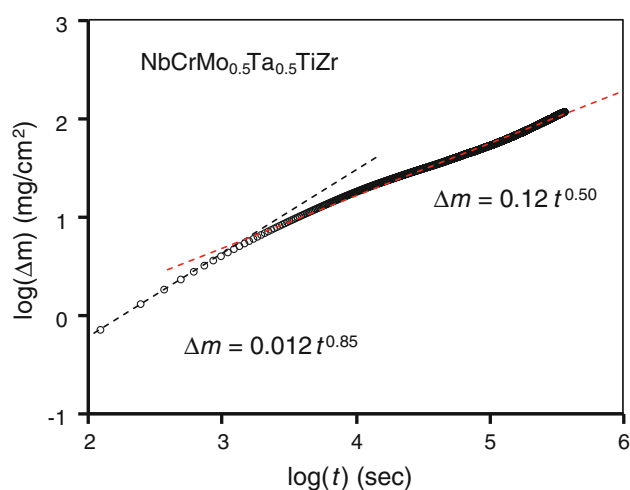


Fig. 15 The logarithmic dependence of the mass gain per the initial surface area of the NbCrMo_{0.5}Ta_{0.5}TiZr alloy sample on the time of oxidation in dry air at 1273 K. Dashed trendlines correspond to equations shown in the figure

evaporation of the MoO_2 from the oxide scale should be known. Unfortunately, we do not know this kinetics. However, one may assume that the kinetics of evaporation is much faster than the oxidation kinetics and that the kinetics of formation of the MoO_2 in the studied alloy is controlled by the kinetics of oxidation of the alloy itself. Using these assumptions, a corrected oxidation behavior has been modeled and the corrected data are given in Fig. 16. The corrected oxidation behavior is described by Eq. (1) with $n = 0.6$ and $k_1 = 0.071 \text{ mg}\cdot\text{cm}^{-2}\cdot\text{s}^{-0.6}$. One can see that the weight correction resulted in a slight increase in the rate constant, k_1 , but it did not change the time exponent. Thus, the oxidation mechanism of the studied alloy discussed at the beginning of this section is likely not affected by the partial evaporation of molybdenum oxides.

Comparison with conventional and developmental refractory alloys

The major problem with conventional Mo alloys is low melting points and volatile behavior of molybdenum oxides, which lead to a rapid loss in weight and catastrophic failure at temperatures greater than $\sim 873 \text{ K}$ [21, 22]. New developmental Mo alloys based on molybdenum silicides and containing boron show considerably improved oxidation resistance at temperatures greater than 1273 K ; however, oxidation is still accompanied by weight loss and substantial weight loss still occurs during air exposure at lower temperatures [21, 23].

Nb-based conventional refractory alloys have extremely poor oxidation resistance at elevated temperatures because

of high oxygen solubility and diffusivity in the Nb matrix and protective coatings are absolutely necessary for these alloys [16, 24–26]. Without protective coating, oxidation of these alloys occurs very rapidly, with considerable weight gain, which generally exceeds $0.04 \text{ mg}/\text{cm}^2/\text{s}$ ($150 \text{ mg}/\text{cm}^2/\text{h}$), followed by alloy embrittlement and disintegration. Several developmental Nb alloys with improved oxidation resistance, containing Ti, Si, Al, and some other elements, have recently been reported [27–29]. Unfortunately, these developmental alloys contain high volume fractions of silicides and aluminides and are brittle at temperatures less than $\sim 1000 \text{ K}$. The results of isothermal oxidation at 1273 K of these developmental alloys are given in Table 6. The oxidation data for pure Nb and our $\text{NbCrMo}_{0.5}\text{Ta}_{0.5}\text{TiZr}$ alloy are also given there. Comparison of the data given in Table 6 indicates that the oxidation resistance of the $\text{NbCrMo}_{0.5}\text{Ta}_{0.5}\text{TiZr}$ alloy is much better than that of the Nb Al, Nb Si, Nb Si Al, and Nb Si Al Ti alloys, as well as Nb 13Si 4Mo and Nb 19Si 5Mo alloys, and similar to that of the Nb 18Si 26Mo alloy. However, oxidation resistance of the developmental Nb 12Si 15Mo alloy [29] is slightly better than that of our alloy.

Oxidation reactions

Oxidation of the high-entropy refractory $\text{NbCrMo}_{0.5}\text{Ta}_{0.5}\text{TiZr}$ alloy is accompanied by only limited diffusion of the alloying elements and leads to formation of complex oxides. No element separation and/or preferable metal oxide formation occur during oxidation. The diffusion distances of the alloying elements are estimated to be less than 500 nm , so that morphologies and compositions of the former BCC1, BCC2, and Laves phases retain while oxidation of these phases is accompanied by large volume expansion. This behavior is somewhat different from the oxidation behavior of conventional Nb alloys, as well as developmental Nb Si Al Ti alloys, where a preferable metal oxide scale forms resulting in a decrease in the concentration of the alloying elements inside the Nb matrix, an increase in the oxygen solubility and eventually internal oxidation [15, 28]. Reduced diffusion rates of the alloying elements in high-entropy alloys were noted in previous publications [6, 12, 13] and it was attributed to a reduced concentration of free vacancies in these multi-principal-element alloys. One may, therefore, conclude that the restricted diffusion of the alloying elements may contribute to formation of many complex oxides in the $\text{NbCrMo}_{0.5}\text{Ta}_{0.5}\text{TiZr}$ alloy. It is also likely that the large number of complex oxides results from the high concentrations of many elements, each of which is a strong oxide former. Because of heavy alloying, low solubility and slow diffusion of oxygen in the alloy are also expected. Indeed, no oxygen was detected in the core part of the oxidized

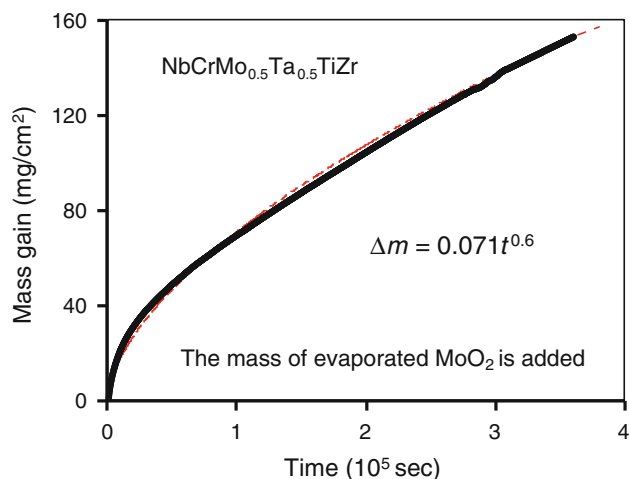


Fig. 16 The corrected dependence of the mass gain per the initial surface area of a $\text{NbCrMo}_{0.5}\text{Ta}_{0.5}\text{TiZr}$ alloy sample on the oxidation time during oxidation in continuously flowing dry air at 1273 K , after adding the estimated mass of the evaporated MoO_2 . Dashed trendline corresponds to the equation given in the figure

Table 6 Weight gain per unit surface area (in mg/cm²) of Nb and several Nb based developmental alloys during isothermal holding at 1273 K in air

Alloy/time	1 h	2 h	4 h	24 h	100 h	Ref
Nb	159	300				[29]
Nb 10Si	37					[29]
Nb 10.1Si	45	90	170			[28]
Nb 17.3Al	23	43	65			[28]
Nb 5Si 9Al	90	160	275			[28]
Nb 7Si 9Al	69	145	275			[28]
Nb 8Si 9Al 10Ti				182	338	[28]
Nb 10Si 9Al 10Ti				95	291	[28]
Nb 6Si 11Al 15Ti				51	167	[28]
Nb 8Si 11Al 15Ti				51	153	[28]
Nb 19Si 5Mo	26	53	106			[29]
Nb 18Si 26Mo	9.7	13.8	19.5	45		[29]
Nb 13Si 4Mo	48	105	166			[29]
Nb 12Si 15Mo	1.3	1.4	4.0	15		[29]
NbCrMo0.5Ta0.5TiZr	10	15	22	50	119	This work

sample at the distances of $\sim 150\ \mu\text{m}$ or higher from the oxide matrix interface. The effective diffusivity of oxygen in the oxidized alloy can be estimated by taking into account that holding at 1273 K for 100 h results in the complete oxidation of $\sim 0.65\text{-mm}$ thick layer and partial oxidation of the 0.15-mm thick transition layer. This gives the effective coefficient for oxygen diffusion through the oxide/alloy at 1273 K, $D_{\text{O}} \approx 3.0 \times 10^{-9}\ \text{cm}^2/\text{s}$. This is two orders of magnitude lower than the oxygen diffusion in pure Nb [30, 31].

Conclusions

Oxidation behavior of a refractory NbCrMo_{0.5}Ta_{0.5}TiZr alloy during heating at 1273 K for 100 h in flowing air was studied. Before oxidation, the alloy consisted of three phases, BCC1, BCC2, and FCC (Laves). The volume fractions of these phases were ~ 67 , 16, and 17 %, respectively. The BCC1 and Laves phases were presented in the form of particles embedded in the continuous BCC2 phase. The BCC1 phase was enriched with Mo, Nb, and Ta, the BCC2 phase was enriched with Zr and Ti, and the FCC Laves phase was enriched with Cr and Zr.

The rate of weight gain per unit surface area during oxidation at 1273 K followed a near-parabolic dependence, $\Delta m = k_1 t^n$, with $n = 0.6$ and $k_1 = 0.055\ \text{mg cm}^{-2}\ \text{s}^{-n}$. This is an indication of formation of protective oxide scale on the sample surface. After 100 h holding at 1273 K, the thickness of the oxide scale was $\sim 1.75\ \text{mm}$.

During cooling from 1273 K to room temperature, separation of the oxide layer from the non-oxidized core

part of the sample occurred. X-ray diffraction of the separated layer showed that it consisted of many complex oxides. Microstructural and EDS analysis of the oxide layer revealed redistribution of the alloying elements at a scale level of less than 500 nm, indicating slow diffusion of these elements during oxidation. Evaporation of volatile molybdenum oxide decreased the concentration of Mo in the oxide layer and formed microporosity inside the former BCC1 particles. Cracks oriented almost parallel to the sample surface developed in the regions of the former BCC2 and Laves phases. The cracks were also extended into the former BCC1 particles, however in much smaller fraction, indicating that the BCC1 phase was more resistant to cracking during oxidation than the two other phases.

About $150\text{-}\mu\text{m}$ thick partially oxidized transition layer was observed under the oxide layer. In this region, oxygen concentration rapidly decreased from the concentration typical to the oxide layer to zero. This concentration profile was described as a sum of two Gaussian distributions, $C_{\text{O}} = A \exp\left[-\frac{x^2}{2Dt}\right]$, where x is the distance from the oxide layer/matrix interface toward the sample center, $2A$ is the oxygen concentration at the interface, and $Dt = 100$ and $2500\ \mu\text{m}^2$ for the first and second distributions, respectively. Such behavior was explained by slower oxygen diffusion in the BCC1 phase than in two other phases.

Acknowledgements Technical support from Drs. Carmen Carney and Fred Meisenkothen is greatly appreciated. This work was supported through the Air Force Research Laboratory Director's Fund and through USAF contract No. FA8650 10 5226.

References

- Dimiduk DM, Perepezko JH (2003) MRS Bull 28:639–645
- MacKay RA, Gabb TP, Smialek JL, Nathal MV (2009) Alloy design challenge: development of low density superalloys for turbine blade applications, NASA/TM 2009 215819
- Subramanian PR, Mendiratta MG, Dimiduk DM, Stucke MA (1997) Mater Sci Eng A2390240:1–13
- Bewlay BP, Jackson MR, Zhao J C, Subramanian PR (2003) Metall Mater Trans A 34A:2043–2052
- Perepezko JH (2009) Science 326(5956):1068–1069
- Senkov ON, Wilks GB, Miracle DB, Chuang CP, Liaw PK (2010) Intermetallics 18:1758–1765
- Senkov ON, Wilks GB, Scott JM, Miracle DB (2011) Intermetallics 19:698–706
- Senkov ON, Scott JM, Senkova SV, Miracle DB, Woodward CF (2011) J Alloys Comp 509:6043–6048
- Senkov ON, Scott JM, Senkova SV, Miracle DB, Woodward CF (2010) J Mater Sci. doi:[10.1007/s10853-012-6260-2](https://doi.org/10.1007/s10853-012-6260-2)
- Senkov ON, Woodward CF (2011) Mater Sci Eng, A 529:311–320
- Yeh J W, Chen S K, Lin S J, Gan J Y, Chin T S, Shun T T, Tsau C H, Chang S Y (2004) Adv Eng Mater 6(5):299–303
- Yeh J W (2006) Annales de Chimie: Science des Matériaux 31:633–648
- Yeh J W, Chen Y L, Lin S J, Chen S K (2007) Mater Sci Forum 560:1–9
- Pint BA, DiStefano JR, Wright IG (2006) Mater Sci Eng, A 415:255–263
- Perkins RA, Chiang KT, Meier GH (1988) Scripta Metall 22:419–424
- Subramanian PR, Mendiratta MG, Dimiduk DM, Stucke MA (1997) Mater Sci Eng A239 240:1–13
- Birks N, Meier GH (1983) Introduction to high temperature oxidation of metals. Edward Arnold (Publishers) Ltd, London
- Kubaschewski O, Hopkins BE (1962) Oxidation of metals and alloys, 2nd edn. Butterworth and Co. Ltd, London
- West JM (1980) *Basic corrosion and oxidation*. Ellis Horwood Limited, Chichester, 1980
- Bernstein HL (1987) Metall Trans A 18A:975–985
- Harwood JJ (1956) Materials and Methods 44(6):84–89
- Mendiratta MG, Parthasarathy TA, Dimiduk DM (2002) Intermetallics 10:225–232
- Meyer M, Kramer M, Akinc M (1996) Adv Mater 8(1):85–88
- Perkins RA, Meier GH (1990) JOM 42(8):17–21
- Jackson MR, Bewlay BP, Rowe RG, Skelly DW, Lipsitt HA (1996) JOM 48(1):39–44
- Yao D, Zhou C, Yang J, Chen H (2009) Corros Sci 51:2619–2627
- Menon ESK, Mendiratta MG, Dimiduk DM (2001) In: Hemker KJ, Dimiduk DM, Clemens H, Darolia R, Inui H, Larsen JM, Sikka VK, Thomas M, Whittenberger JD (eds) Structural Intermetallics TMS, Materials Park, pp 591–600
- Murayama Y, Hanada S (2002) Sci Tech Adv Mater 2:145–156
- Chattopadhyay K, Mitra R, Ray KK (2008) Metall Mater Trans A 39A:577–592
- Perkins RA, Padgett RA Jr (1977) Acta Metall 25:1221–1230
- Farraro RJ, McLellan RB (1978) Mater Sci Eng 33:113–116